Mechanism-Based and Input-Output Modeling of the Key Neuronal Connections and Signal Transformations in the CA3-CA1 Regions of the Hip....

7 authors, including:

Kunling Geng
University of Southern California
7 PUBLICATIONS   **19** CITATIONS

Dae C Shin
University of Southern California
58 PUBLICATIONS   **563** CITATIONS

Dong Song
University of Southern California
204 PUBLICATIONS   **2,374** CITATIONS

Robert Hampson
Wake Forest School of Medicine
205 PUBLICATIONS   **7,968** CITATIONS

Some of the authors of this publication are also working on these related projects:

Neural Interface Technology View project

Models of cerebral hemodynamics as diagnostic markers of dementia View project

Mechanism-Based and Input-Output Modeling of the Key Neuronal Connections and Signal Transformations in the CA3-CA1 Regions of the Hippocampus

Kunling Geng
kgeng@usc.edu
Dae C. Shin
shind@usc.edu
Dong Song
dsong@usc.edu
Department of Biomedical Engineering and the Biomedical Simulations Resource Center at the University of Southern California, Los Angeles, CA, 90089, U.S.A.

Robert E. Hampson
rhampson@wfubmc.edu
Samuel A. Deadwyler
sdeadwyl@wfubmc.edu
Department of Physiology and Pharmacology, Wake Forest School of Medicine, Winston-Salem, NC, 27157, U.S.A.

Theodore W. Berger
berger@bmsr.usc.edu
Vasilis Z. Marmarelis
vzm@usc.edu
Department of Biomedical Engineering and the Biomedical Simulations Resource Center at the University of Southern California, Los Angeles, CA, 90089, U.S.A.

This letter examines the results of input-output (nonparametric) modeling based on the analysis of data generated by a mechanism-based (parametric) model of CA3-CA1 neuronal connections in the hippocampus. The motivation is to obtain biological insight into the interpretation of such input-output (Volterra-equivalent) models estimated from synthetic data. The insights obtained may be subsequently used to interpretat input-output models extracted from actual experimental data. Specifically, we found that a simplified parametric model may serve as a useful tool to study the signal transformations in the hippocampal CA3-CA1 regions. Input-output modeling of model-based synthetic data show that GABAergic interneurons are responsible for regulating neuronal excitation, controlling the precision of spike timing, and maintaining network oscillations, in a manner consistent with previous studies. The input-output model obtained from real data exhibits intriguing

similarities with its synthetic-data counterpart, demonstrating the importance of a dynamic resonance in the system/model response around 2 Hz to 3 Hz. Using the input-output model from real data as a guide, we may be able to amend the parametric model by incorporating more mechanisms in order to yield better-matching input-output model. The approach we present can also be applied to the study of other neural systems and pathways.

1 Introduction

The hippocampus is one of the most important brain structures because it plays a critical role in episodic memory formation (Scoville & Milner, 1957; Tulving & Markowitsch, 1998), learning (Berry & Thompson, 1978; Whitlock, Heynen, Shuler, & Bear 2006), and spatial navigation (O'Keefe & Nadel, 1978; Moser, Moser, Forrest, Andersen, & Morris, 1995). The CA3 and CA1 regions of the hippocampus have been extensively studied because of the synaptic plasticity exhibited in their circuitry, such as the Schaffer collateral pathway (Collingridge, Kehl, & McLennan, 1983; Bliss & Collingridge, 1993). Another reason is that the CA3 and CA1 regions are vulnerable to many diseases (Small, Schobel, Buxton, Witter, & Barnes, 2011). For example, neuron loss in the CA3 and CA1 regions of the hippocampus is common in Alzheimer's disease (West, Coleman, Flood, & Troncoso, 1994; Padurariu, Ciobica, Mavroudis, Fotiou, & Baloyannis, 2012). Therefore, studying the signal transformations in CA3 and CA1 regions is crucial for understanding the function of the hippocampus and eventually building a neuroprosthesis to reconstruct the neural connections and restore impaired memory formation (Berger et al., 2001, 2012; Hampson et al., 2012, 2013).

The circuitry of the CA3 and CA1 regions is rather complex. As shown in Figure 1, the CA1 pyramidal cells receive excitatory inputs from the entorhinal cortex via the perforant pathway (PP) and the CA3 cells via the Schaffer collaterals (SC). The PP synapses are located at the distal apical dendrites, and the SC synapses are at the proximal dendrites (Otmakhova, Otmakhov, & Lisman, 2002; Andersen, 2007). Recent research indicates that some hippocampal GABAergic interneurons such as oriens lacunosum-moleculare (OLM) cells would facilitate the transmission from CA3 while reducing the influence of entorhinal cortex (Leão et al., 2012). In this letter, we consider only the signal transformations from the CA3 region to the CA1 region; the inputs from the entorhinal cortex are not included in our model. In the CA1 region, the principal cells receive not only excitatory glutamatergic inputs but also inhibitory GABAergic inputs, which originate mainly from interneurons (Freund & Buzsáki, 1996). Although the local GABAergic interneurons are a small proportion of the total number of neurons, they are responsible for regulating the excitation, controlling the precision of spike
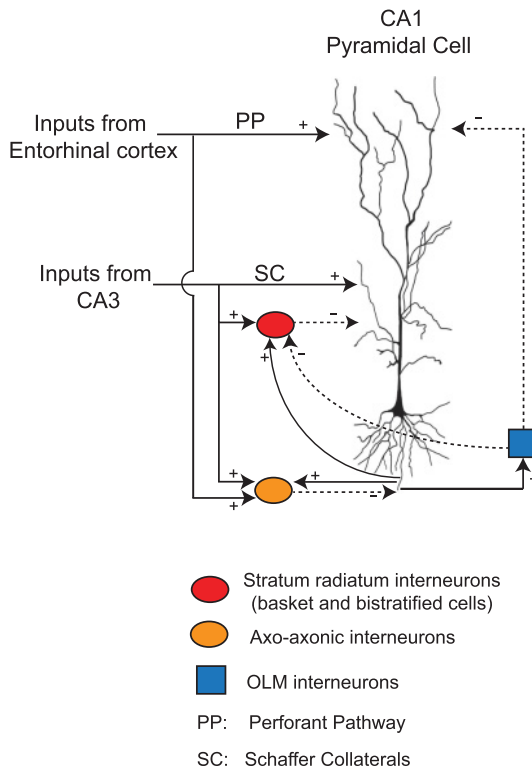
Figure 1: Schematic of the neural circuit of a CA1 cell in the hippocampus.

timing, and maintaining network oscillations (Sik, Penttonen, Ylinen, & Buzsáki, 1995; Fricker & Miles, 2001; Mann & Paulsen, 2007; Klausberger, 2009; Kullmann, 2011; Andersen, 2007). The interneurons are highly diverse and can be classified morphologically, neurochemically, and physiologically (McBain & Fisahn, 2001; Maccaferri & Lacaille, 2003). The CA1 pyramidal cells receive inhibitory GABAergic inputs from interneurons, such as basket, bistratified, axo-axonic, and oriens lacunosum-moleculare (OLM) cells. The basket and bistratified cells target the proximal apical dendrites, while the axo-axonic cells target the axons of CA1 cells. All of these cells take part in both feedforward and feedback inhibitory circuits (Sik et al., 1995; McMahon & Kauer, 1997; Cutsuridis, Cobb, & Graham, 2010; Müller & Remy, 2014). In this study, we ignore the axo-axonic interneurons, because 92% of the GABAergic synapses contact CA1 cells via their proximal dendrites (Megias, Emri, Freund, & Gulyas, 2001). The OLM interneurons, which act only in the feedback circuits, are found to inhibit the distal

apical dendrites as well as disinhibit the proximal apical dendrites of CA1 cell (Leão et al., 2012).

Previously nonparametric input-output modeling methods, such as multiple-input multiple-output (MIMO) Volterra modeling, have been utilized to analyze the signal transformations between the CA3 and CA1 regions (Zanos et al., 2008; Sandler et al., 2015a, 2015b; Song et al., 2007, 2013, 2016). Although these methods provide valuable predictive models in a nonlinear dynamic context, they do not offer much insight into the underlying biological mechanisms. On the other hand, detailed compartmental models have been developed in an effort to represent the signal transformations within CA1 circuits (Cutsuridis, Cobb, & Graham, 2010; Olypher, Lytton, & Prinz, 2012). However, this task is daunting because of the difficulty in incorporating all the biological details of the diversity and complexity of synaptic plasticity (Malenka & Bear, 2004; Andersen, 2007), dendritic structure (Spruston, Schiller, Stuart, & Sakmann, 1995), neuronal backpropagation (Golding, Kath, & Spruston, 2001), and interneuron connections (Maccaferri & Lacaille, 2003). In this letter, we simplify the model of CA3-to-CA1 signal transformations to represent the essential mechanisms and the associated neural circuitry between CA3 and CA1, as shown in Figure 2. The simplified structural/parametric model consists of six modules, which we describe in section 2.

In order to evaluate the model with synthetic and experimental data, we use a newly developed data-based method, neuronal mode network (NMN), which can be used to analyze either synthetic data generated from simulations of the model in Figure 2 or actual experimental data. NMN is capable of extracting the dynamics and the static nonlinearities in neural systems under minimum assumptions. Comparing NMN results from synthetic data with NMN results from experimentally collected data in the human hippocampus, we can evaluate the simplified CA3-CA1 model of Figure 2 and gain insight into the origin of the dynamics and nonlinearities contained within the experimental data.

The organization of this letter is as follows. We first introduce the simplified structural/parametric CA3-CA1 model, which consists of six modules, in section 2. Then we give the basic descriptions of the nonparametric data-based modeling method NMN in section 3. The simulation results and analysis are shown in section 4. The discussion and conclusions are given in section 5.

2 Parametric Model of CA3-CA1 Signal Transformation

2.1 Schaffer Collateral Presynaptic Model. The presynaptic activities introduce the use-dependent plasticity such as short-term depression and facilitation within the timescale from milliseconds to seconds (Dittman, Kreitzer, & Regehr, 2000; Zucker & Regehr, 2002). This short-term presynaptic plasticity is critical for neural information processing, such as regulation
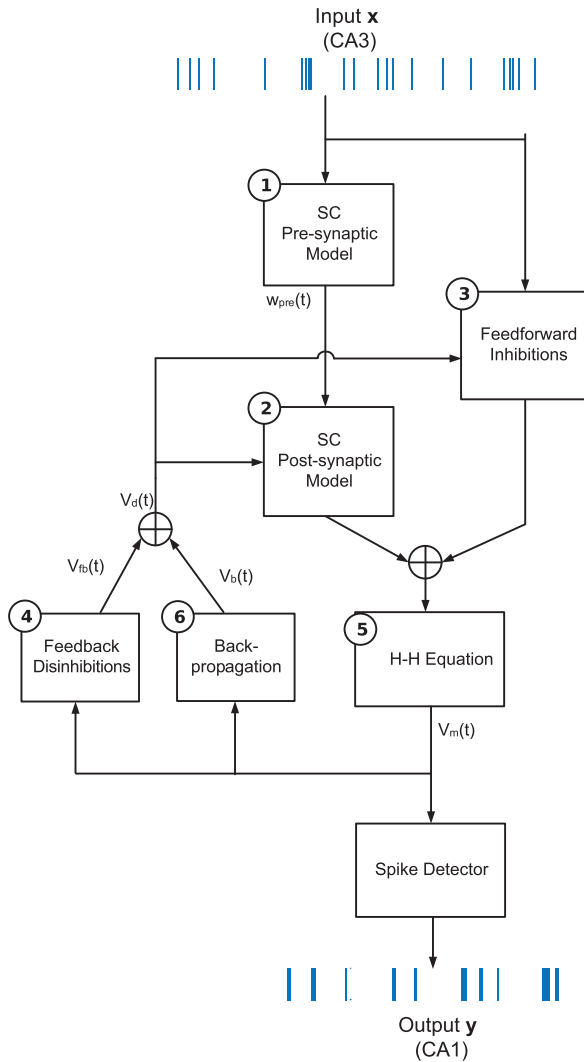
Figure 2: Structure of simplified CA3-CA1 structural/parametric model.

of the circuit properties in SC (Pouille & Scanziani, 2004; Regehr, 2012) and the function as an adaptive filter for high-frequency discharges (Klyachko & Stevens, 2006; Kandaswamy, Deng, Stevens, & Klyachko, 2010). In order to model the short-term plasticity, we adopt the classic Dittman's model based on the residual calcium hypothesis (Dittman et al., 2000), which has also been used for comparison with nonparametric Volterra models (Song,

Marmarelis, & Berger, 2009). The short-term plasticity of the is expressed as the presynaptic weight

$$w_{pre}(t) = F(t)D(t) \tag{2.1}$$

where $F(t)$ represents the facilitation factor and $D(t)$ is the depression factor, both ranging from 0 to 1. $F(t)$ is described by the equations

$$F(t) = F_1 + \frac{1 - F_1}{1 + K_F/CaX_F(t)}, \tag{2.2}$$

$$\frac{\partial CaX_F}{\partial t} = -CaX_F(t)/\tau_F + \Delta_F \cdot \delta(t - t_0), \tag{2.3}$$

$$K_F/\Delta_F = \frac{1 - F_1}{\rho F_1/(1 - F_1) - F_1} - 1, \tag{2.4}$$

where F_1 is the baseline probability of transmitter release and CaX_F is the concentration of the putative calcium-bound molecule, which decays with time constant τ_F after a surge of Δ_F at time t_0 when an action potential occurs. $\delta(t)$ is the Dirac delta function. K_F is the affinity of CaX_F. K_F and Δ_F follow the relation shown in equation 2.4, where ρ is the facilitation ratio.

The depression factor $D(t)$ is defined by

$$\frac{\partial D}{\partial t} = (1 - D(t)) \cdot k_{recov}(CaX_D) - D(t) \cdot F(t) \cdot \delta(t - t_0), \tag{2.5}$$

$$\frac{\partial CaX_D}{\partial t} = -CaX_D(t)/\tau_D + \Delta_D \cdot \delta(t - t_0), \tag{2.6}$$

$$k_{recov}(CaX_D) = \frac{k_{max} - k_0}{1 + K_D/CaX_D(t)} + k_0, \tag{2.7}$$

where k_{recov} is the rate of recovery that is bounded by k_0 and k_{max}. CaX_D is the concentration of another putative calcium-bound molecule, which decays with time constant τ_D after a surge of Δ_D at time t_0 when an action potential occurs. K_D is the affinity of CaX_D. We adopt the SC presynaptic parameters from Dittman et al. (2000), which are summarized in Table 1.

2.2 Schaffer Collateral Postsynaptic Model. After the neurotransmitters are released in the presynaptic sites, they diffuse across the synaptic cleft and reach the postsynaptic membrane, activating the respective synaptic channels and producing the postsynaptic currents. Glutamate is the main excitatory neurotransmitter in the SC pathway, where the AMPA receptor (AMPAr) and the NMDA receptor (NMDAr) are the main ionotropic receptors for glutamate (Dingledine, Borges, Bowie, & Traynelis, 1999). The AMPAr mediates the fast excitatory postsynaptic potentials (EPSPs), while the NMDAr mediates the slow EPSPs (Destexhe, Mainen, & Sejnowski, 1994).

Table 1: Parameters of the SC Presynaptic Model.

ρ	2.2
F_1	0.24
τ_F	100 ms
Δ_F	1
τ_D	50 ms
k_{max}	0.03 ms^{-1}
k_0	0.002 ms^{-1}
K_D	2
Δ_D	1

The nonlinear current-voltage $(I - V)$ relationship of the NMDAr reflects the blockage of Mg^{2+} at the resting potential, which is crucial for the coincidence detector since the activation of the NMDAr requires both the presynaptic glutamate release and the postsynaptic membrane depolarization (Tsien, Huerta, & Tonegawa, 1996). The dynamics of the AMPAr conductance can be expressed as the classic biexponential equation (Destexhe et al., 1994; Kleppe & Robinson, 1999; Dayan & Abbott, 2001):

$$g_{APMAr}(t) = g_{\max\_AMPAr} B_{AMPAr}(e^{-t/\tau_1} - e^{-t/\tau_2}) \tag{2.8}$$

where $g_{\max\_AMPAr}$ is the maximum conductance of the AMPAr, τ_1 and τ_2 are the relevant time constants, and $B_{AMPAr} = 1/[(\tau_2/\tau_1)^{\tau_2(\tau_1-\tau_2)} - (\tau_2/\tau_1)^{\tau_1(\tau_1-\tau_2)}]$ is the normalizing factor, which guarantees that the conductance would reach its maximum value $g_{\max\_AMPAr}$.

The dynamics of the NMDAr conductance can also be expressed in the biexponential form (Kapur, Lytton, Ketchum, & Haberly, 1997; Wang, Song, & Berger, 2002):

$$g_{NMDAr}(t) = g_{\max\_NMDAr} B_{NMDAr} \frac{e^{-t/\tau_3} - e^{-t/\tau_4}}{1 + \eta[Mg^{2+}]e^{-\gamma V_d(t)}} \tag{2.9}$$

where $g_{\max\_NMDAr}$ is the maximum conductance of the NMDAr, τ_3 and τ_4 are the related time constants, and $B_{NMDAr} = 1/[(\tau_4/\tau_3)^{\tau_4(\tau_3-\tau_4)} - (\tau_4/\tau_3)^{\tau_3(\tau_3-\tau_4)}]$ is the normalizing factor; $[Mg^{2+}]$ is the concentration of Mg^{2+}, and $V_d(t)$ is the dendritic membrane potential; η and γ are constants related to the voltage-dependent Mg^{2+} blockage.

The EPSCs of the AMPAr and NMDAr can be expressed by the convolutional relations

$$I_{APMAr}(t) = n_{AMPAr}(w_{pre}(t) \otimes g_{AMPAr}(t))(V_d(t) - E_{rev\_AMPAr}), \tag{2.10}$$

$$I_{NMDAr}(t) = n_{NMDAr}(w_{pre}(t) \otimes g_{NMDAr}(t))(V_d(t) - E_{rev\_NMDAr}), \tag{2.11}$$

Table 2: Parameters of AMPAr and NMDAr.

g_{max_AMPAr}	10 pS
τ_1	1 ms
τ_2	0.4 ms
E_{rev_AMPAr}	0 mV
g_{max_NMDAr}	30 pS
τ_3	55 ms
τ_4	0.6 ms
η	0.33 mM^{-1}
γ	0.14 mV^1
E_{rev_NMDAr}	0 mV

where n_{AMPAr} and n_{NMDAr} are the numbers of AMPAr and NMDAr, respectively; w_{pre} is the presynaptic weight calculated from equation 2.1; and $\otimes$ represents the convolution operator. E_{rev_AMPAr} and E_{rev_NMDAr} are the reverse potentials of the AMPAr and NMDAr, respectively. All the parameters of AMPAr and NMDAr are summarized in Table 2 (adapted from Wang et al., 2002).

2.3 Feedforward Inhibition. As shown in Figure 1, the feedforward interneurons of the CA3-to-CA1 circuit include bistratified, basket, and axo-axonic cells (Cutsuridis, Cobb, & Graham, 2010). To simplify our model, we treat only the feedforward interneurons as a module rather than model them separately. We also omit the interactions between interneurons such as the mutual inhibitions between bistratified and basket cells (Andersen, 2007; Cutsuridis, Cobb, & Graham, 2010; Saudargiene, Cobb, & Graham, 2015). The feedforward inhibition module in Figure 2 receives input from the CA3 cell and generates the IPSPs that are integrated by the CA1 dendrites. For the feedforward inhibitions, the plasticity of interneurons (Kullmann & Lamsa, 2007; Ali, 2011) is not considered in this model. The IPSPs generated by feedforward inhibition for GABA$_A$ and GABA$_B$ receptors are described by the convolutional relations,

$$I_{ff\_GABAAr}(t) = n_{ff\_GABAAr}[x(t - t_d) \otimes g_{GABAAr}(t)][V_d(t) - E_{rev\_GABAAr}],$$
(2.12)

$$I_{ff\_GABABr}(t) = n_{ff\_GABABr}[x(t - t_d) \otimes g_{GABABr}(t)][(V_d(t) - E_{rev\_GABABr}],$$
(2.13)

where n_{ff_GABAAr} and n_{ff_GABABr} are the numbers of GABA$_A$ and GABA$_B$ receptors for the feedforward inhibitions, t_d is the time delay introduced by interneurons, E_{rev_GABAA} and E_{rev_GABAB} are the reverse potentials, and V_d is the membrane potential of the dendrites. The conductances of the GABA$_A$

Table 3: Parameters of GABAAr and GABABr.

$g_{\max\_GABAAr}$	70 pS
τ_5	8 ms
τ_6	1 ms
E_{rev_GABAAr}	−70 mV
$g_{\max\_GABABr}$	40 pS
τ_7	100 ms
τ_8	35 ms
E_{rev_GABABr}	−70 mV
t_d	2 ms

and GABA$_B$ receptors are expressed as the biexponential functions

$$g_{GABAAr}(t) = g_{\max\_GABAAr} B_{GABAAr}(e^{-t/\tau_5} - e^{-t/\tau_6}), \tag{2.14}$$

$$g_{GABABr}(t) = g_{\max\_GABABr} B_{GABABr}(e^{-t/\tau_7} - e^{-t/\tau_8}), \tag{2.15}$$

where $g_{\max\_GABAA}$ and $g_{\max\_GABAB}$ are the maximum conductances; B_{GABAAr} and B_{GABABr} are normalizing factors that guarantee that the conductances reach their maximum values; and τ_5, τ_6, τ_7, τ_8 are time constants. The parameters of the GABA$_A$ and GABA$_B$ receptor are adopted from Cutsuridis, Graham, Cobb, and Vida (2010) and Gauck and Jaeger (2003), which are summarized in Table 3.

2.4 Feedback Disinhibition. One of the most important types of feedback interneurons in the hippocampus is the OLM cell, which receives excitatory inputs from the axon collaterals of the CA1 cells (Cutsuridis, Cobb, & Graham, 2010; Saudargiene et al., 2015). The OLM interneurons are found to inhibit the distal apical dendrites and disinhibit the proximal apical dendrites of the CA1 cell. Therefore, the information flow from the SC pathway is enhanced, while the information flow from the entorhinal cortex is suppressed (Leão et al., 2012; Müller & Remy, 2014; Womelsdorf, Valiante, Sahin, Miller, & Tiesinga, 2014). As shown in Figure 1, the stratum raditaum and axo-axonic interneurons not only provide feedforward inhibitions but also participate in the feedback inhibitions. The effects of axo-axonic interneurons are excluded because of the relatively small number of GABAergic synapses on axons (Megias et al., 2001). In this module, we do not include the feedback inhibition effects caused by stratum raditaum interneurons because the feedforward inhibitions play a more important role (Paz & Huguenard, 2015; Ferrante & Ascoli, 2015). The inhibitory effects on the distal dendrites caused by OLM cells are also not included in the feedback module in Figure 2 because the amplitudes of IPSPs attenuate dramatically as the dendrites are located farther away from the soma (Spruston, 2008). Therefore, the feedback module only includes the OLM

disinhibition effects on the proximal dendrites, which introduce the additional membrane potential depolarization (Leão et al., 2012). This depolarization caused by OLM cells is quantified by the equations:

$$V_{fb} = V_{fb\_GABAAr} + V_{fb\_GABABr}, \tag{2.16}$$

$$V_{fb\_GABAAr}(t) = n_{fb\_GABAAr}[V_m(t - t_d) - E_{rev\_GABAAr}] \otimes g_{GABAAr}(t)R, \tag{2.17}$$

$$V_{fb\_GABABr}(t) = n_{fb\_GABABr}[V_m(t - t_d) - E_{rev\_GABABr}] \otimes g_{GABABr}(t)R, \tag{2.18}$$

where n_{fb_GABAAr} and n_{fb_GABABr} are the numbers of GABA$_A$ and GABA$_B$ receptors for the feedback disinhibitions, t_d is the time delay introduced by interneurons, and R is the resistance of the dendrites, which is chosen as 1Ω without loss of generality.

2.5 Synaptic Integration and the H-H Model. Each CA1 neuron receives numerous synaptic inputs from different locations, which spread at different distances from the soma. The resulting EPSPs and IPSPs from synapses are location dependent (Allam et al., 2015). In order to simplify the integration of the synaptic currents, we use a uniform synapse model rather than treat each synapse differently, as shown in sections 2.3 and 2.4. Therefore, the dendritic membrane potential V_d in our model is treated as the integrated value rather than the membrane potential from a specific synapse. To model the dynamic processes for the generation of an action potential (AP) by a CA1 cell, we adopt the classic Hodgkin-Huxley (H-H) equations (Hodgkin & Huxley, 1952). The total current injected into the H-H model is

$$I(t) = -[I_{AMPAr}(t) + I_{NMDAr}(t) + I_{ff\_GABAAr}(t) + I_{ff\_GABABr}(t)]. \tag{2.19}$$

The main H-H equation is

$$I = C_m \frac{dV}{dt} + g_{max\_K} n^4 (V - E_K) + g_{max\_Na} m^3 h(V - E_{Na})$$
$$+ g_{max\_L}(V - E_L), \tag{2.20}$$

where V is the membrane potential and C_m is the membrane capacitance. The maximum conductances of potassium sodium, and leakage ion channel are represented by g_{max_K}, g_{max_Na}, and g_{max_L}. E_K, E_{Na}, E_L are the reverse potentials for each channel. We use the standard H-H parameters from the giant axon of a squid, which are summarized in Table 4. The gating variables m, n, h are responsible for the voltage-dependent activation and deactivation of the channels, which are described by the first-order differential

Table 4: Parameters of the H-H Equations.

C_m	1 uF/cm^2
E_K	-12 mV
E_{Na}	115 mV
E_L	10.6 mV
g_{max_K}	36 mS/cm^2
g_{max_Na}	120 mS/cm^2
g_{max_L}	0.3 mS/cm^2

equations:

$$\frac{dn}{dt} = \alpha_n(1 - n) - \beta_n n, \tag{2.21}$$

$$\frac{dm}{dt} = \alpha_m(1 - m) - \beta_m m, \tag{2.22}$$

$$\frac{dh}{dt} = \alpha_h(1 - h) - \beta_h h, \tag{2.23}$$

$$\alpha_n(V) = \frac{-0.01(V - 10)}{e^{-(V-10)/10} - 1}, \; \beta_n(V) = 0.125 e^{-V/80}, \tag{2.24}$$

$$\alpha_m(V) = \frac{-0.1(V - 25)}{e^{-(V-25)/10} - 1}, \; \beta_m(V) = 4 e^{-V/18}, \tag{2.25}$$

$$\alpha_h(V) = 0.07 e^{-V/20}, \; \beta_h(V) = \frac{1}{e^{-(V-30)/10} + 1}. \tag{2.26}$$

It should be noted that the resting potential is 0 mV; thus, we have to calibrate the resting potential by adding the offset voltage, so that the membrane potential of the soma/axon is

$$V_m = V + V_{offset} \tag{2.27}$$

where V_{offset} is chosen as -65 mV, which matches the experiments in vivo (Henze & Buzsaki, 2001).

2.6 Backpropagation of Action Potential. After the action potential (AP) is initiated in the axon of the CA1 cell, it will backpropagate to the dendritic branches (Stuart, Spruston, Sakmann, & Häusser, 1997). Backpropagation (BP) is hypothesized to provide the necessary depolarization to remove the Mg^{2+} block of the NMDAr channels, which is essential for induction of long-term potentiation (Stuart et al., 1997; Johnston et al., 2003). Another effect of BP is to reset the synaptic integration by depolarizing the dendritic membrane potential close to the reverse potential of glutamate receptors (Stuart et al., 1997; Häusser, Major, & Stuart, 2001). One approach
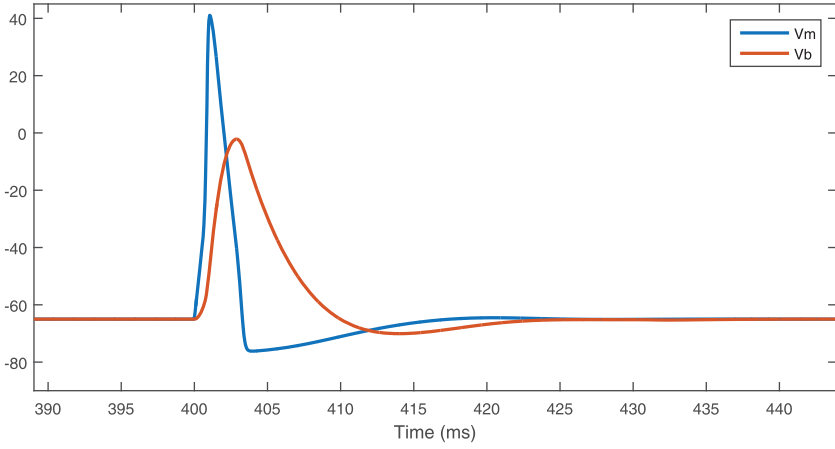
Figure 3: Illustration of the simplified backpropagation model, where V_m is the membrane potential of the soma/axon and V_b is the backpropagating potential.

to model the BP is based on the cable theory and compartment models based on the realistic morphology of dendrites and axons (Larkum, Rioult, & Lüscher, 1996; Lüscher & Larkum, 1998). To simplify the BP model, we assume that the BP action potentials are produced by convolving the membrane potential from soma/axon with a low-pass filter, and the amplitude of the backpropagating AP is attenuated by a certain proportion,

$$V_b = \beta[V(t) \otimes e^{-t/\tau}] + V_{offset}, \tag{2.28}$$

where β is the shrinkage factor and τ is the time constant of BP. We choose $\beta = 0.5$, $\tau = 5$ ms to approximate the realistic BP effects (Stuart et al., 1997), as illustrated in Figure 3. It should be noted that the activity-dependent properties (Spruston et al., 1995) and dichotomous behavior of the back-propagating APs (Golding et al., 2001) in CA1 cells are not included in our BP module. The membrane potential of the dendrites in the CA1 cell V_d is

$$V_d(t) = V_b + V_f. \tag{2.29}$$

3 The Input-Output Model: Neuronal Model Network

In order to evaluate the mechanism-based structural model and compare it with the actual experimental data, we use a newly developed data-based method, the neuronal mode network (NMN), in order to analyze the data generated from the parametric model shown in Figure 2. The NMN method stems from the Volterra-equivalent network (Marmarelis & Zhao, 1997;
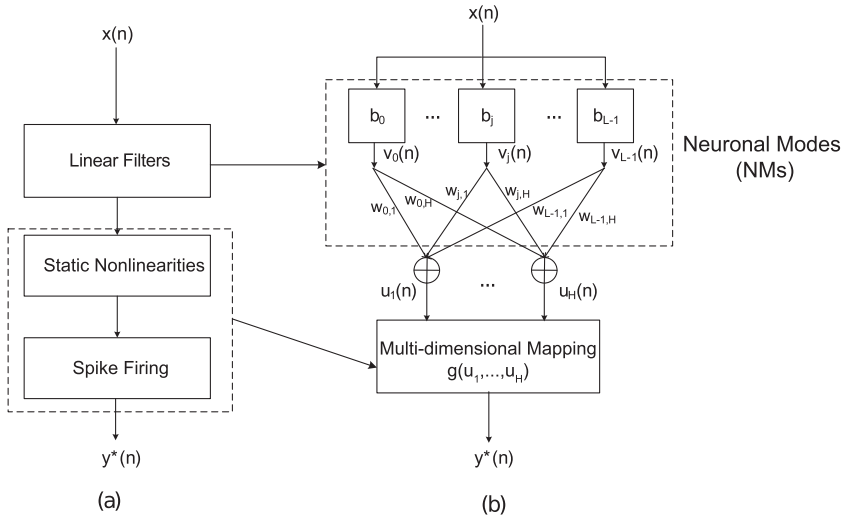
Figure 4: The architecture of (a) the traditional cascade model and (b) NMN. The NMs are linear filters and the MDM nonlinearly transforms the outputs of NMs into firing probabilities.

Marmarelis, 2004; Geng & Marmarelis, 2015, 2017) and is capable of extracting the dynamics and the static nonlinearities in neural systems under minimum assumptions. As shown in Figure 4, the NMN follows the general framework of the classic cascade model (Marmarelis & Marmarelis, 1978; Dayan & Abbott, 2001; Marmarelis, 2004). Compared with the modeling method using principal dynamic modes (PDMs) (Marmarelis & Orme, 1993; Marmarelis, 1997; Marmarelis et al., 2013, 2014) and the widely used approach of generalized linear models (Paninski, 2004; Truccolo, Eden, Fellows, Donoghue, & Brown, 2005), the NMN would offer improved model estimation and prediction results.

As illustrated in Figure 4, the NMN consists of two cascaded stages, a set of near-optimal linear filters, the neuronal modes (NMs), and the multi-dimensional mapping (MDM) that nonlinearly transforms the NM output combinations into firing probabilities. The objective of NMN is to find a set of NMs in order to separate the combinations of NM output values that cause an output spike from combinations that do not. This separation between the two states of the output is described by the estimated MDM. The NMs of the system can be represented as the weighted sum of discrete Laguerre function (DLF) b_j that serve as basis functions:

$$p_h(m) = \sum_{j=0}^{L-1} w_{j,h} b_j(m),$$ (3.1)

$$b_j(m) = \alpha^{(m-j)/2}(1-\alpha)^{1/2} \sum_{k=0}^{j} (-1)^k \binom{m}{k}\binom{j}{k} \alpha^{j-k}(1-\alpha)^k, \qquad (3.2)$$

where α is the Laguerre parameter, which controls the exponential declining rate of DLF. The outputs of the NMs can be expressed as

$$u_h(n) = \sum_{m=0}^{M-1} p_h(m)x(n-m),$$

$$= \sum_{m=0}^{M-1}\sum_{j=0}^{L-1} w_{j,h}b_j(m)x(n-m),$$

$$= \sum_{j=0}^{L-1} w_{j,h}v_j(n), \qquad (3.3)$$

where $v_j(n)$ is the convolution between the input $x(n)$ and the respective DLF:

$$v_j(n) = \sum_{m=0}^{M-1} b_j(m)x(n-m). \qquad (3.4)$$

The MDM transforms the NM outputs into a firing probability by a multi-dimensional histogram according to Bayes' rule:

$$y^*(n) = p[y(n) = 1|u_1(n), u_2(n), \ldots, u_H(n)]$$

$$\propto \frac{p[u_1(n), u_2(n), \ldots, u_H(n)|y(n) = 1]}{p[u_1(n), u_2(n), \ldots, u_H(n)]}. \qquad (3.5)$$

Figure 5 is an illustration of how to construct the MDM. Let u_1 and u_2 be the outputs of the two NMs and use (u_1^*, u_2^*) and (u_1', u_2') to represent the NM output combinations that cause an output spike or not, respectively. The scatter plot of all (u_1^*, u_2^*) and (u_1', u_2') points is shown in Figure 5b. The scatter plot has $N_{gd} \times N_{gd}$ pixels, and the number of (u_1^*, u_2^*) and (u_1', u_2') falling in each pixel (s_1, s_2) is denoted as $N_p(s_1, s_2)$ and $N_z(s_1, s_2)$, respectively. The firing probability corresponding to each pixel can be calculated as

$$g(s_1, s_2) = \frac{N_p(s_1, s_2)}{N_p(s_1, s_2) + N_z(s_1, s_2)}. \qquad (3.6)$$

We use a "heat map" in Figure 5c to represent the MDM. The red areas correspond to high firing probability, which is termed the trigger region
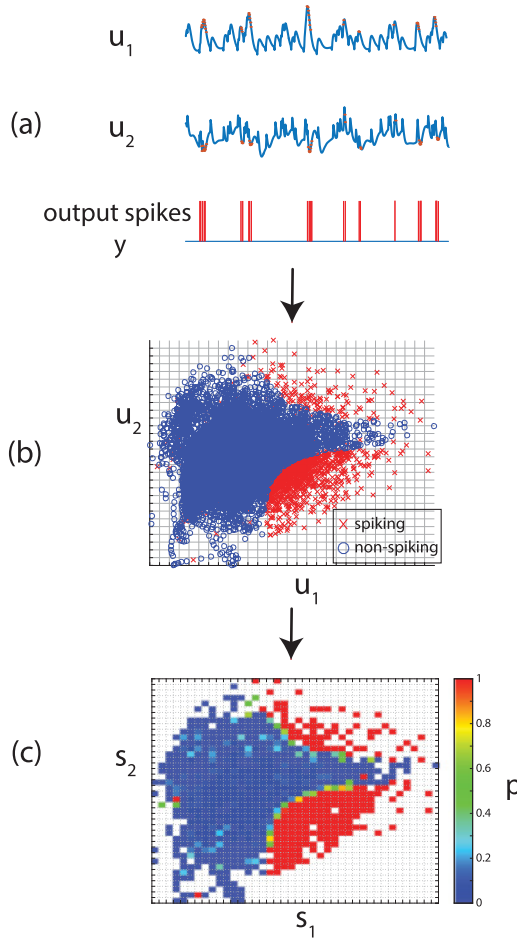
Figure 5: Illustration of MDM. (a) The outputs of *NMs* $u_1(n)$ and $u_2(n)$. The red points (u_1^*, u_2^*) represent the combination of NM output values leading to output spikes y. The unmarked points (u_1', u_2') represent the combination of NM output values corresponding to zero output. (b) The scatter plot of the spiking points (u_1^*, u_2^*) and the nonspiking points (u_1', u_2'). (c) The constructed MDM after calculating the firing probability (p) in each pixel.

(TR). The blue areas correspond to low firing probability, which is termed the zero region (ZR). In this letter, due to the limited amount of human hippocampus data, we restrict the MDM to be two-dimensional. The details of choosing the cost function and training the NMN model are summarized in appendixes A and B.

Table 5: Numbers of Glutamate and GABA Receptor Channels.

n_{AMPAr}	2.4×10^7
n_{NMDAr}	6×10^6
n_{ff_GABAAr}	1.5×10^7
n_{ff_GABABr}	6×10^6
n_{fb_GABAAr}	1.2×10^6
n_{fb_GABABr}	3×10^5

4 Modeling Results

4.1 Regular Case. In order to generate the output response similar to the regular hippocampal CA1 cell, we need to set appropriate parameters for the number of glutamate and GABA receptors. The ratio of n_{AMPAr}/n_{NMDAr} is chosen as 4:1 according to Hu, Bouteiller, Song, Baudry, and Berger (2015). Since the total number of glutamate receptors and GABA receptors is unknown in a CA1 cell, they should be carefully balanced in order to produce the naturally spiking activity, as shown in Table 5.

The input x is generated by the homogeneous Poisson model (Heeger, 2000), and the mean firing rate is 4.37 spikes/sec. The responses of each module in the system are shown in Figure 6. The mean firing rate of the output y is 4.78 spikes/sec. As shown in Figure 6, the presynaptic short-term plasticity plays an important role in regulating the synaptic strength. For example, from 6800 ms to 6900 ms, two spikes in the CA3 cell fire very closely and cause a significant drop of synaptic strength, which prevents the CA1 cells from being overexcited. In the postsynaptic module, AMPAr and NMDAr mainly contribute to the excitatory currents, but they also contribute to the brief inhibitory currents when the dendritic membrane potential V_d surpasses the reverse potential of AMPAr and NMDAr (0 mV), which would reset the excitatory currents after the AP backpropagates to the dendrites. The feedforward GABAAr inhibitory currents are fast and transient, which reduces the potential firing shortly after the generation of AP, while the GABABr inhibitory currents are slow and enduring, which reduces the firing after a relatively long time period.

Then we feed the input x and output y into the NMN model to obtain the system dynamic (NMs) and nonlinearity (MDM). Figure 7 shows the NMs and MDMs, which are obtained from the simulated data and from actual data collected in the human hippocampus during the intraoperative performance of a delayed match-to-sample task. The experiment details and the key NMN analysis results of the collected human hippocampus data are described in appendix C. Due to the limited amount of the data, it is likely that the SISO NMN analysis would bias toward certain frequency bands, and the estimated NMs and MDMs from the human hippocampus data exhibit high variability (shown in Figures 11 and 12). To mitigate this problem,
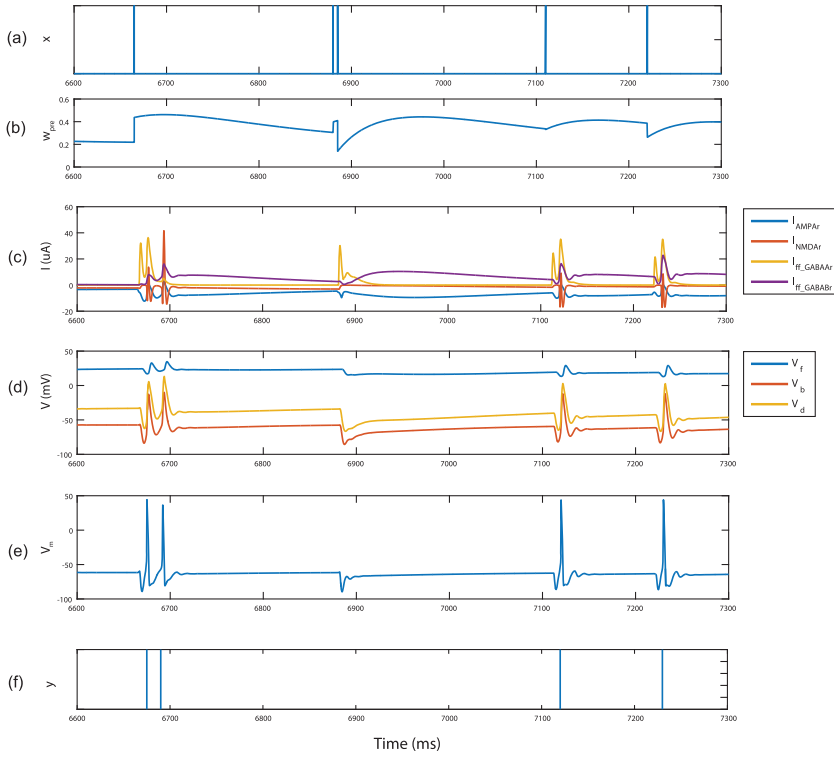
Figure 6: Simulation results of the CA3-CA1 parametric model. (a) The input spikes x of the parametric model. (b) The response of SC presynaptic model. (c) The postsynaptic currents. (d) The backpropagation potential V_b, feedback potential V_f, and dendritic membrane potential V_d. (e) The membrane potential of the dendrite/soma. (f) The output spikes y of the parametric model.

we invoke the concept of global NMs (GNMs) that are obtained via singular value decomposition of the matrix composed of all estimated NMs of the functionally connected input-output neurons. The obtained GNMs of the human hippocampus data are shown in Figure 7 (red solid lines) and represent the common dynamic components of the MIMO neural system that serve as a functional coordinate basis for all neuronal dynamics in the subject system. After substituting the individual NMs with the global NMs, the recalculated MDMs become more regular, shown in Figure 12. The uniform and consistent elliptical shapes may indicate similar underlying mechanisms in the CA3 and CA1 neuronal connections. Therefore, we would like to examine if the simulation results obtained from the synthetic CA3-CA1 system would yield similar NMs and MDMs.
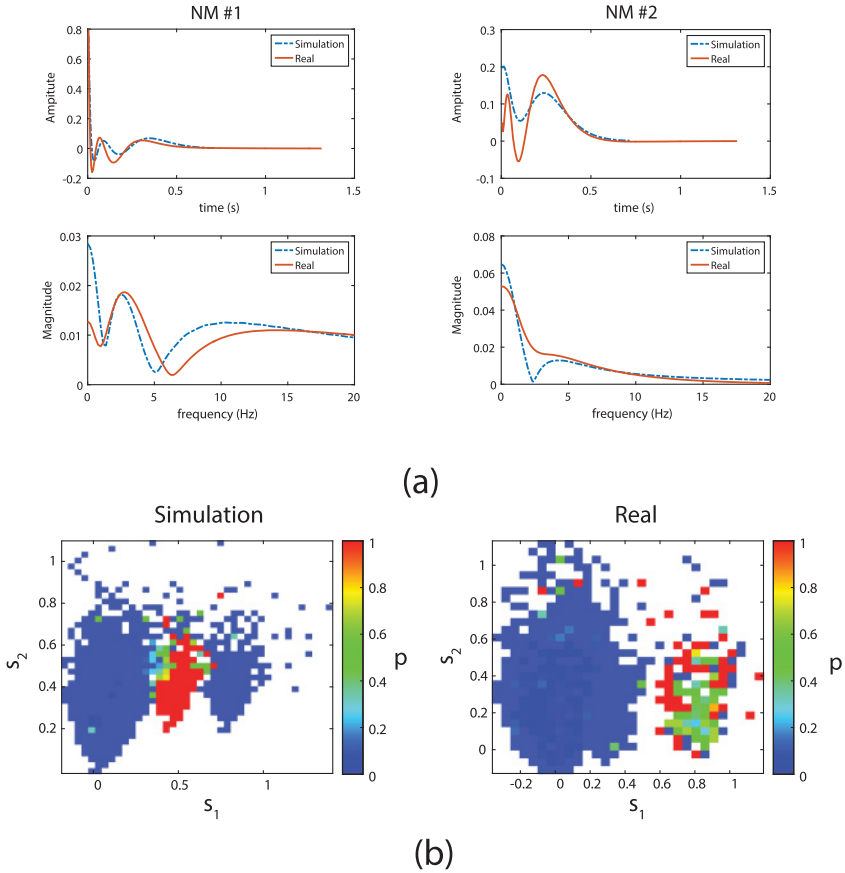
Figure 7: (a) The obtained NMs from the simulated data (blue dashed lines) and real hippocampus data (red solid lines) in the time domain and frequency domain. (b) The obtained MDM from the simulated and the real hippocampus data.

As shown in Figure 7, the NMs and MDMs obtained from the simulated and real data share some intriguing similarities. For example, NM #1 from simulated and real data exhibits a resonant peak around 3 Hz and a similar high-pass characteristic. The TRs and ZRs from both the simulated and real data are well separated with respect to the output of NM #1, although there is an additional ZR for the simulated data at higher values of the output of NM #1.

4.2 Deactivation of Feedback Disinhibition. Research studies have shown a significant loss of OLM cells in epilepsy (Cossart et al., 2001;
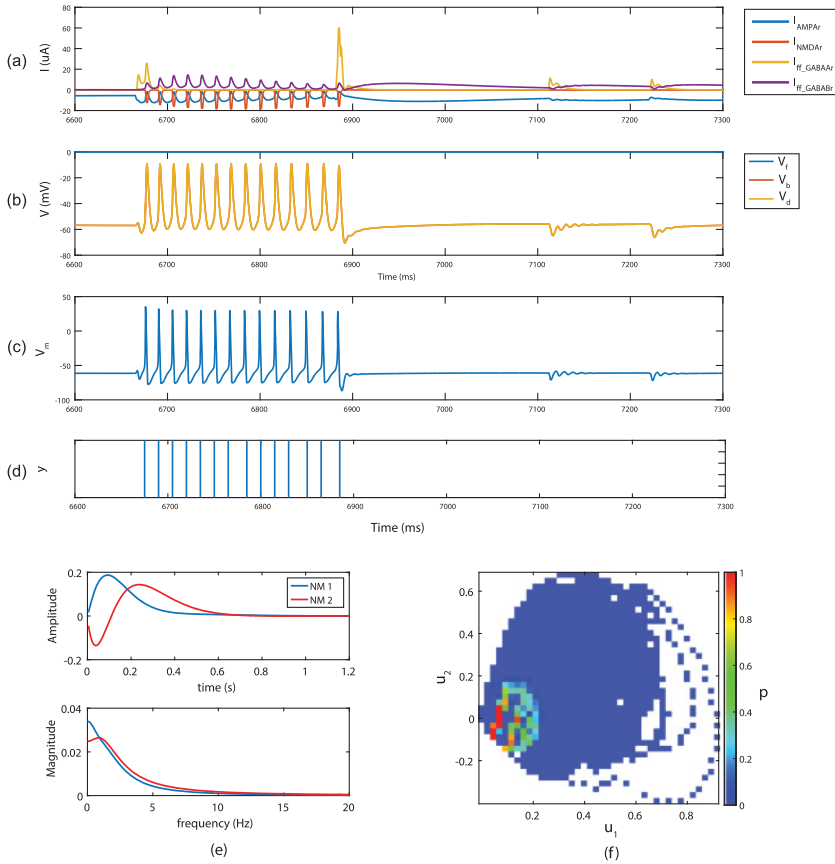
Figure 8: Simulation results of the CA3-CA1 parametric model when the feedback disinhibition module is disabled. (a) The postsynaptic currents. (b) The backpropagation potential V_b, feedback potential V_f, and dendritic membrane potential V_d. (c) The membrane potential of the dendrite/soma. (d) The output spikes of the parametric model. (e) The obtained NMs. (f) The obtained MDM.

Dinocourt, Petanjek, Freund, Ben-Ari, & Esclapez, 2003). In order to explore how the deactivation of the feedback disinhibition caused by OLM cells loss would affect the output activity of the CA1 cell, as well as the dynamics and nonlinearities of the system, we compute the model response after deactivation of the feedback inhibition module, as shown in Figures 8a to 8d. The output of the CA1 cell shows intermittent bursting with a firing rate of 10.74 spikes/sec. The feedback depolarization potential is 0 mV, and therefore, the dendritic membrane potential V_d is always below the reverse potential of NMDA and AMPA, so that the NMDAr and AMPAr contribute only to

the excitatory currents. Although the feedback disinhibition seems to make the CA1 cell excitatory, the overall effect turns out to be inhibitory. In a comparison of Figure 6c and Figure 8a, the feedback disinhibition would cause the additional depolarizations of the dendrites, push the membrane potential to surpass the reverse potential of NMDAr and AMPAr (0 mV), and cause the transient inhibitory currents. According to Figure 6c, NMDAr plays a dominant role in the transient inhibitory currents because of the nonlinear I-V relationship and slow dynamics of the conductance. The obtained NMs and MDM are shown in Figures 8e and 8f. The obtained NM #1 acts as a low-pass filter, and the NM #2 has a resonance peak around 1 Hz. There are no resonance peaks of the NMs at higher frequencies in this case. Although the obtained TR of the MDM is clearly clustered, it is surrounded by the ZR rather than being well separated as in Figure 7b.

4.3 Deactivation of Feedforward Inhibition. It has been observed that the feedforward inhibition is lost in epilepsy (Paz & Huguenard 2015), so it is important to explore how the removal of feedforward inhibition would affect the behavior of the model. When we remove the feedforward inhibition module in Figure 2 and keep the rest of the parameters the same as section 4.1, the system exhibits sustained bursting output of a very high firing rate of 94.00 spikes/sec, as shown in Figure 9. The feedback disinhibition depolarizes the membrane potential of dendrites and helps to remove the Mg^{2+} blockage of NMDAr and generate more excitatory currents that facilitate the generation of AP. The disinhibition also helps to elevate the dendritic membrane potential to surpass the reverse potential of the glutamate receptors (0 mV) that generate the inhibitory currents. However, the excitatory effects are stronger than the inhibitory effects, and the overall outputs exhibit sustained bursting of spikes. The obtained NMs shown in Figure 9 are elongated and exhibit resonant peaks around 1 Hz, while higher-frequency resonances are absent. The obtained MDM is blurred, and the TR cannot be clearly distinguished from the ZR.

5 Discussion and Conclusion

In this letter, we have introduced a simplified mechanism-based CA3-to-CA1 parametric model (shown in Figure 2) that captures the main neuronal connections and mechanisms that contribute to the signal transformations from the CA3 to the CA1 region in the hippocampus. We have examined each module and provided the underpinnings of the mathematical formulation of the respective parametric model in section 2. In order to evaluate the resulting mechanism-based parametric/structural model, we use a newly developed databased method of input-output modeling, the neuronal mode network (NMN), to obtain an input-output model from the synthetic data generated from the parametric model. The results indicate that the simplified mechanism-based CA3-to-CA1 model exhibits similar input-output
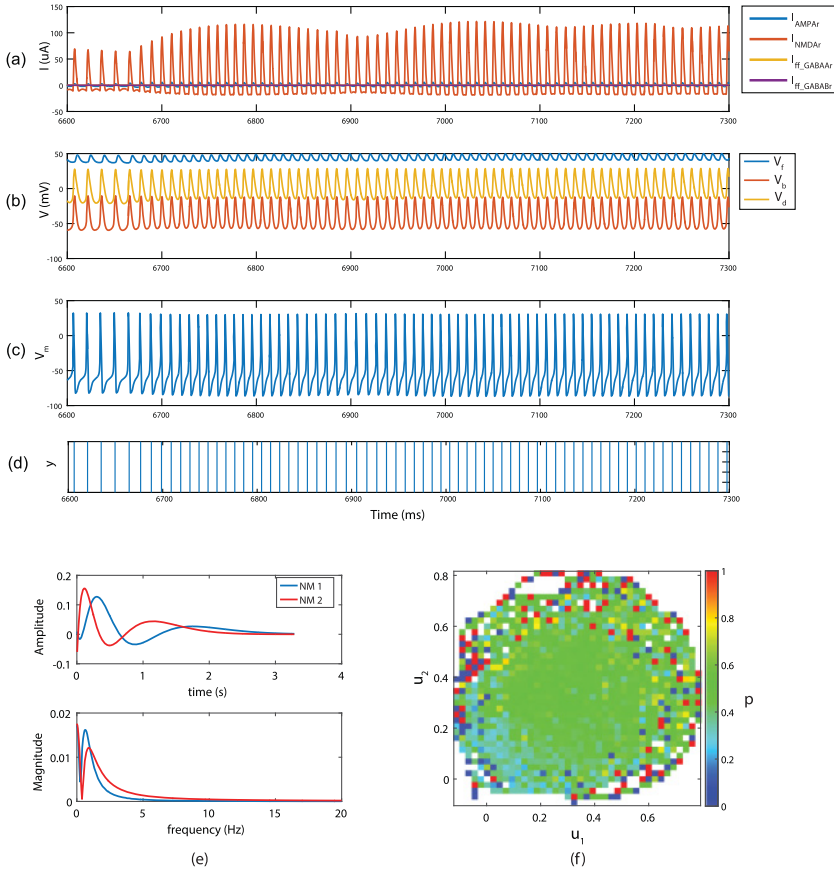
Figure 9: The simulation results of the CA3-CA1 parametric model when the feedforward inhibition module is disabled. (a) The postsynaptic currents. (b) The backpropagation potential V_b, feedback potential V_f, and dendritic membrane potential V_d. (c) The membrane potential of the dendrite/soma. (d) The output spikes of the parametric model. (e) The obtained NMs. (f) The obtained MDM.

system dynamics and nonlinearities as observed using real data collected in the human hippocampus (see Figure 7). Specifically, the obtained MDMs indicate that the NM #1 (with a resonant peak around 2–3 Hz for both synthetic and real data) is mainly responsible for spike generation at the CA1 neuron. However, there are also some discrepancies observed between the input-output (MNM) models obtained from synthetic and real data, which may be caused by the exclusion of inputs from the entorhinal cortex or possible oversimplifications in the parametric model.

The loss of GABAergic interneurons and the dysfunction of hippocampal neural circuits are considered to be responsible for epilepsy (Cossart et al., 2001; Dinocourt et al., 2003; Ang, Carlson, & Coulter, 2006; Ben-Ari, Crepel, & Represa, 2008; Goldberg & Coulter, 2013; Paz & Huguenard, 2015). Thus, it is useful to explore the effects of feedforward inhibition and feedback disinhibition, as discussed in sections 4.2 and 4.3. The results shown in Figures 8 and 9 indicate that the deactivation of either feedforward inhibition or feedback disinhibition causes seizure-like bursting of action potentials (APs). When we compare the results shown in Figures 7 and 8, we can see that the feedback disinhibition effects are not merely excitatory or inhibitory. On one hand, the disinhibition helps the NMDAr to further depolarize in order to remove the Mg^{2+} blockage and generate more excitatory currents that facilitate the generation of AP. On the other hand, the disinhibition helps to reduce the bursting of APs by elevating the dendritic membrane potential to surpass the reverse potential of the glutamate receptors (0 mV) that would reset the excitatory currents after the AP backpropagates to the dendrites.

When we compare the results from Figures 7 and 9, we can see that the feedforward inhibition effects are essential to prevent the overbursting activity of the CA1 cell. Using the NMN as the tool to analyze the data, we found that the neural dynamics concentrated on the very low-frequency bands (<1 Hz) and higher-frequency dynamics are absent in both cases, which indicate that the feedforward inhibition together with feedback disinhibition are essential for modulating the oscillations in the CA3-to-CA1 signal transformation process. Comparing Figures 8f and 9f with 7a, we can see that another role of the GABAergic interneurons is to maintain the separation of the TR and ZR in the MDM, which is critical in order to preserve the spiking timing precision.

In summary, the simplified parametric model shown in Figure 2 may serve as a useful tool to study the signal transformations in the hippocampal CA3-CA1 regions. The results in Figures 8e and 9e indicate that deactivation of the feedback disinhibition module and feedforward inhibition module would lead to different dynamics/resonant frequencies of the system compared with the actual data in Figure 7a. In addition, Figures 8c and 8d, and 9c and 9d, suggest that significant loss of interneurons would cause the epileptic activities, since the GABAergic interneurons are responsible for regulating neuronal excitation, controlling the precision of spike timing, and maintaining network oscillations, in a manner consistent with previous research studies (Sik et al., 1995; Fricker & Miles, 2001; Mann & Paulsen, 2007; Klausberger, 2009; Kullmann, 2011; Andersen, 2007). The input-output models obtained from simulated/synthetic and real data exhibit similarities in demonstrating the importance of a dynamic resonance in the system/model response around 2 Hz to 3 Hz (see Figure 7). Recent studies also have shown that the "slow-theta" in the human hippocampus

(around 3 Hz) is evident when the subjects are performing the episodic memory task and virtual navigation task (Lega, Jacobs, & Kahana, 2012; Watrous, Fried, & Ekstrom, 2011; Watrous et al., 2013; Jacobs, 2014). However, the neural rhythms of slow-theta oscillations observed in EEG recordings or local field potentials are collected activities of a large population of neurons rather than the single pair of CA3-CA1 neurons. One limitation of our current model is that it focuses on the signal transformation of a single pair of CA3-CA1 neurons, which may not able to represent all the dynamics of the hippocampal systems. In the future, a population model needs to be further implemented to explore the genesis of oscillations in the hippocampus, especially the theta-gamma coupling relationships (Kopell, Börgers, Pervouchine, Malerba, & Tort, 2010; Lisman & Jensen, 2013). In addition, the approach could be extended to the study of the dynamics of the hippocampal neural network in well-characterized conditions, such as a pair of place cells (O'Keefe & Burgess, 1996) or concept cells (Quiroga, 2012).

Appendix A: Cost Function of NMN

The objective of training the NMN is to find a set of near-optimal NMs that separate the spiking points (u_1^*, u_2^*) from the nonspiking points (u_1', u_2') in the MDM. The parameters we need to optimize are $\{w_{j,h}\}$ and α, which determine the shapes and time span of NMs. The cost function should be carefully selected to quantize the separation between the spiking and nonspiking points. We propose a cost function adapted from the Ising model (Ising, 1925) and Potts model (Wu, 1982), which is defined as

$$J = -\beta \sum_{\langle i, j \rangle} g(i)g(j), \tag{A.1}$$

where $\beta = N_{gd}^{-1}$ is the normalization factor and $g(i)$ is the firing probability at the ith pixel, which is defined in equation 3.6. The notation $\langle i, j \rangle$ represents the bonds formed by neighboring pixels i and j, which is illustrated in Figure 3. This Ising energy cost function encourages the clustering of spiking points (u_1^*, u_2^*) to form TR, because the cost function is reduced if both $g(i)$ and $g(j)$ are large (see Figure 10). In addition, it discourages the mix between the spiking and nonspiking points. Since the number of spikes and zeros are highly imbalanced, if the spiking and nonspiking points are well mixed, then all the pixels in MDM would have either zero or a very small firing probability, and there is no evident TR formed in MDM. The corresponding Ising energy will be high since $\sum_{\langle i, j \rangle} g(i)g(j) \approx 0$. Thus, by minimizing this Ising cost function, the separation between the spiking and
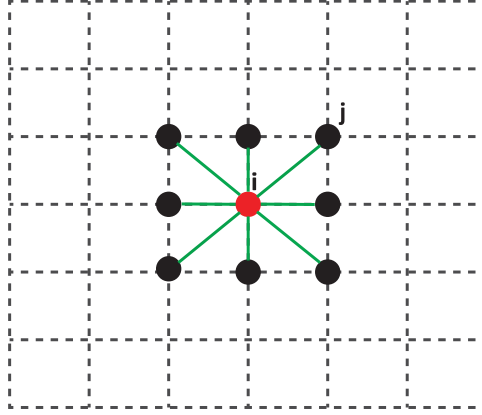
Figure 10: Illustration of the Ising energy. Each dot represents a pixel in MDM. The red dot i has eight nearest neighbors, which are represented by the black dots. The edge between the i and one of the neighbors j forms an energy bond (green line). The total energy is calculated by summing up all the energy bonds in MDM.

nonspiking points is optimized. However, if the input and output have no causal relationship, it is impossible to find a set of optimal NMs that can lead to such separation. In that case, the MDM after optimization would still be largely blurred, there is no evident TR, and the cost function would be around zero. Therefore, the MDM and its associated Ising energy could serve as an indicator of how strongly the input and output are functionally connected. Another important feature of this cost function is that it mitigates the imbalanced class problem of spike train data. The NMN method seeks to find a set of NMs that yield an optimal structure of the MDM instead of directly maximizing the prediction performance (as traditional learning algorithms do) that would suffer from the imbalanced class problem.

Appendix B: Training NMN with Simulated Annealing Algorithm ____

Since the cost function is not differentiable with respect to the parameters that need to be optimized, traditional gradient descent methods like backpropagation cannot be used. Therefore, we propose the use of the simulated annealing (SA) algorithm (Kirkpatrick, Gelatt, & Vecchi, 1983), a global optimization method that does not require gradient information. The SA algorithm has been shown to be suitable for training Volterra-equivalent networks (Geng & Marmarelis, 2017). The following are the basic steps of SA to optimize the parameter set **p**:

1. Randomly initialize the parameter set $\mathbf{p}$, and set the temperature T at a sufficiently large value T_0. In our case, α has to be in the range $(0, 1)$ and the weights $\{w_{j,h}\}$ set within the range $(-1, 1)$.

2. Perform a small random move $\Delta\mathbf{p}$ based on the current parameter set, so that the new one is $\mathbf{p}' = \mathbf{p} + \Delta\mathbf{p}$. In this move, a single parameter p is randomly chosen from the whole set following a uniform distribution, so that each time, every parameter would have the same probability of being selected. Then, p is updated by the following rule,

$$p^{new} = \begin{cases} p + \gamma_p & \text{if } h > 0.5 \\ p - \gamma_p & \text{if } h \leq 0.5 \end{cases}, \tag{B.1}$$

   where the constant γ_p is the step size and h is a random number drawn from a uniform distribution within the range $[0, 1]$.

3. Compute the cost functions $J(\mathbf{p})$ and $J(\mathbf{p}')$, respectively, to get the difference: $\Delta J = J(\mathbf{p}') - J(\mathbf{p})$.

4. Calculate the acceptance probability:

$$r = \begin{cases} 1 & \text{if } \Delta J < 0 \\ e^{-\Delta J/T} & \text{otherwise} \end{cases}, \tag{B.2}$$

   that is, if $\Delta J < 0$, we accept the new parameter set $\mathbf{p}'$; otherwise, $\mathbf{p}'$ is accepted with the probability defined above.

5. Repeat steps 2 to 4 until it reaches an equilibrium, which may be close to a local minimum. In practice, we often choose a large but fixed number of iterations.

6. Decrease the temperature T according to the exponential decay cooling schedule (Nourani & Andresen 1998), where γ in in the range $(0.95, 0.99)$:

$$T(t) = \gamma T(t - 1), \quad t = 1, 2, 3 \ldots \tag{B.3}$$

When the Laguerre parameter α is updated, the outputs of the DLF filter bank $v_j(n)$ are recomputed (see equations 3.2 and 3.4). Since each time α is updated only by decreasing or increasing by a step size γ_α and α is within the range $(0, 1)$, there are only $1/\gamma_\alpha - 1$ possible values. Therefore, we can calculate all the possible values of $v_j(n)$ for each α and store them in a lookup table to reduce the overall computational burden.

If we scale each NM weight $w_{j,h}$ with a constant λ_h and scale the axis of MDM u_h with $1/\lambda_h$, then the overall system still remains the same. Since SA is a stochastic process, the final model trained by SA may have a very large constant λ_h, which will require numerous unnecessary iterations. To avoid

Table 6: Simulated Annealing Parameters.

Symbol	Name	Value
T_0	Initial temperature	100
η	Cooling constant	0.99
N_t	Number of temperature droppings	1500
N_i	Number of iterations at each temperature	200
γ_α, γ_w	Step size	0.01

this problem, we normalize the weights during the training process as

$$w_{j,h} = \frac{w_{j,h}}{\sqrt{\sum_{j=0}^{L-1} w_{j,h}^2}} \tag{B.4}$$

so that

$$\sum_{j=0}^{L-1} w_{j,h}^2 = 1. \tag{B.5}$$

With this normalization, the efficiency of the training process is largely improved. It should be mentioned that the estimation results are not sensitive to SA-related parameters, and SA can provide only near-optimal results (Geng & Marmarelis, 2017). The parameters of the SA training process used in this letter are summarized in Table 6.

Appendix C: Human Hippocampus Data

Multineuronal data were recorded from the CA3 and CA1 regions of the human hippocampus intraoperatively in medically refractory focal epilepsy patients at the Wake Forest Baptist Medical Center. All procedures were reviewed and approved by the Institutional Review Board of Wake Forest University, in accordance with the National Institutes of Health. Patients underwent preoperative imaging to determine intraoperative electrode placement. The FDA-approved electrodes are capable of single-unit neuronal recording and field potential recording (Ad-Tech Medical Instrumentation Corporation, Racine, WI). Intraoperative placement of the depth electrodes was performed using either a stereotactic head frame (CRW Precision Arc, Integra Life Sciences, Plainsboro, NJ) or frameless stereotactic system (VarioGuide, Brainlab AG, Feldkirchen, Germany) at the discretion of the operating surgeon. Hippocampal electrode placement was targeted to penetrate the head of the hippocampus perpendicular to its long axis in order to record neuronal activity within the CA3 and CA1 subfields. The data are recorded intraoperatively during the delayed match-to-sample

(DMS) task. The DMS trials were initiated by the examiner who manually triggered the presentation of a nonverbalizable image, constituting the sample presentation (SP) phase of the task. Completion of the SP task required the patient to touch the presented image, designated as the sample response (SR) phase.

The SR phase then initiated the delay interval phase of the trial during which the screen was blank for 5 to 15 seconds, randomly determined on a trial-by-trial basis. The delay interval was followed by the match presentation (MP) phase of the task, which consisted of the simultaneous display of two to seven images displayed at randomly selected spatial locations on the screen, one of which was the sample image. Touching either the previously presented image or another image was designated a match response (MR). Correct responses produced a reward tone followed by a blank screen. Incorrect responses caused by touching one of the nonmatch (distractor) images constituted a nonmatch response led to an error tone followed by a blank screen. Trials were separated by 5 seconds prior to initiation of the next trial. Single-unit neural activities from 10 patients were recorded and isolated using the Blackrock Cervello Elite electrophysiological recording system with a raw data acquisition frequency at 30,000 samples/sec without filtering. We set the frequency of the automatic spike-sorting algorithm at 30,000 samples/sec with 500 to 5000 Hz bandpass filtering.

We present the results of NMN analysis of data only from patient No. 2 as a pilot study. For patient No. 2, 14 trials were recorded with the correct DMS response and 22 trials with the incorrect response. Spike train data were recorded from seven CA3 neurons and eight CA1 neurons during the DMS task.

We analyzed the data during the 7 sec period after SP, with a bin size of 5 ms. We applied the NMN approach to determine the functional connectivity between the CA3 neurons as inputs and the CA1 neurons as outputs. Fifty-six neuronal input-output pairs were analyzed. Because of the observed variability of the estimated NMs and MDMs in Figure 11, we invoke the concept of global NMs (GNMs) that are obtained via singular value decomposition of the matrix composed of all estimated first or second NMs of the functionally connected input-output neurons, which is akin to the concept of global PDMs (Marmarelis et al., 2013, 2014). The obtained first and second GNMs are shown in Figure 7a and represent the common dynamic components of the MIMO neural system that serves as a functional coordinate basis for all neuronal dynamics in the subject system. We see that the first GNM peaks at around 3 Hz and 15 Hz, while the second GNM exhibits a low-pass characteristic. The new MDMs that are computed based on the obtained GNMs are shown in Figure 12 for the correct DMS responses. We can see that the TRs and ZRs are mainly separated by the first NM output, so this NM seems to be the important one for these neuronal pairs. The uniform and consistent elliptical shapes may indicate similar underlying mechanisms in the CA3 and CA1 neuronal connections.
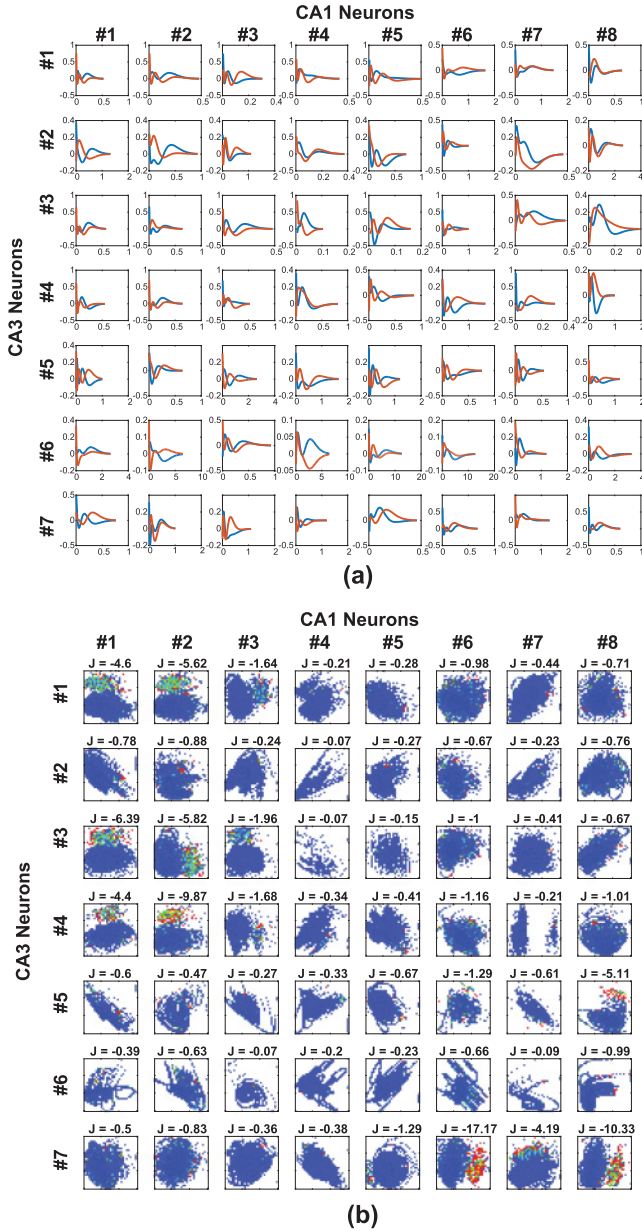
(a)

(b)

Figure 11: (a) The NMs and estimated from NMN for the human hippocampus training data. The unit of *x*-axis is in seconds. The blue curves represent the NM 1 and red curves represent the NM 2. (b)The corresponding estimated MDMs, where J represents the energy function of NMN in equation A.1.
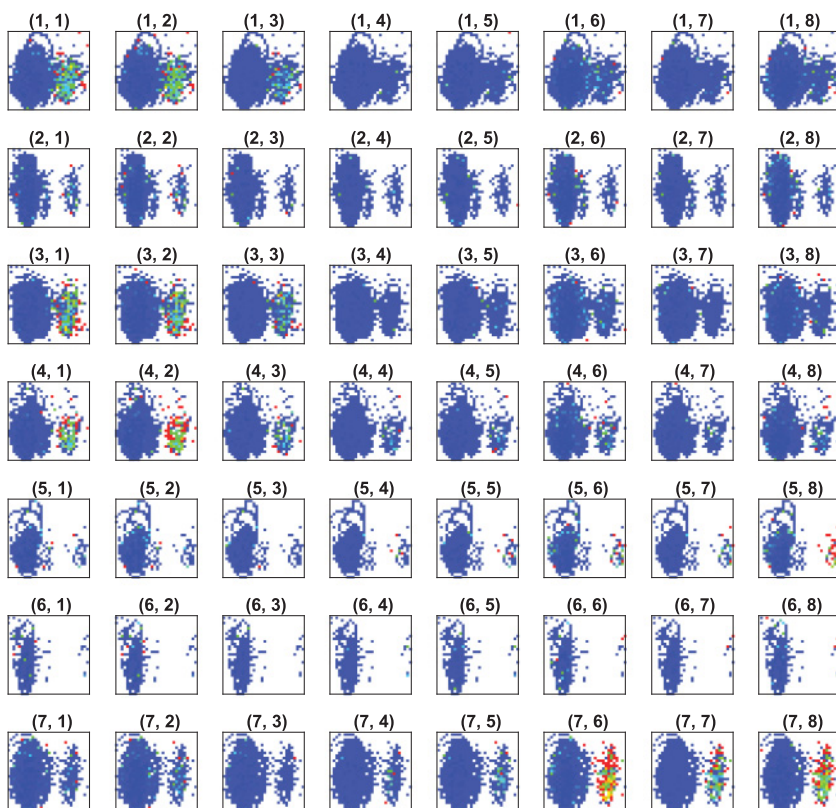
Figure 12: The new MDMs computed based on the GNMs of hippocampus CA3-to-CA1 data.

References

Ali, A. B. (2011). CB1 modulation of temporally distinct synaptic facilitation among local circuit interneurons mediated by N-type calcium channels in CA1. *Journal of Neurophysiology*, *105*(3), 1051–1062.

Allam, S. L., Bouteiller, J. M. C., Hu, E. Y., Ambert, N., Greget, R., Bischoff, S., . . . Berger, T. W. (2015). Synaptic efficacy as a function of ionotropic receptor distribution: A computational study. *PloS One*, *10*(10), e0140333.

Andersen, P. (Ed.). (2007). *The hippocampus book*. New York: Oxford University Press.

Ang, C. W., Carlson, G. C., & Coulter, D. A. (2006). Massive and specific dysregulation of direct cortical input to the hippocampus in temporal lobe epilepsy. *Journal of Neuroscience*, *26*(46), 11850–11856.

Ben-Ari, Y., Crepel, V., & Represa, A. (2008). Seizures beget seizures in temporal lobe epilepsies: The boomerang effects of newly formed aberrant kainatergic synapses. *Epilepsy Currents*, *8*(3), 68–72.

Berger, T. W., Baudry, M., Brinton, R. D., Liaw, J., Marmarelis, V. Z., Park, A. Y., . . . Tanguay, A. R. (2001). Brain-implantable biomimetic electronics as the next era in neural prosthetics. *Proceedings of the IEEE*, *89*(7), 993–1012.

Berger, T. W., Song, D., Chan, R. H., Marmarelis, V. Z., LaCoss, J., Wills, J., . . . Granacki, J. J. (2012). A hippocampal cognitive prosthesis: Multi-input, multi-output nonlinear modeling and VLSI implementation. *IEEE Transactions on Neural Systems and Rehabilitation Engineering*, *20*(2), 198–211, doi:10.1109/TNSRE .2012.2189133

Berry, S. D., & Thompson, R. F. (1978). Prediction of learning rate from the hippocampal electroencephalogram. *Science*, *200*(4347), 1298–1300.

Bliss, T. V., & Collingridge, G. L. (1993). A synaptic model of memory: Long-term potentiation in the hippocampus. *Nature*, *361*(6407), 31–39.

Collingridge, G. L., Kehl, S. J., & McLennan, H. T. (1983). Excitatory amino acids in synaptic transmission in the Schaffer collateral-commissural pathway of the rat hippocampus. *Journal of Physiology*, *334*(1), 33–46.

Cossart, R., Dinocourt, C., Hirsch, J. C., Merchan-Perez, A., De Felipe, J., Ben-Ari, Y., . . . Bernard, C. (2001). Dendritic but not somatic GABAergic inhibition is decreased in experimental epilepsy. *Nature Neuroscience*, *4*(1), 52–62.

Cutsuridis, V., Cobb, S., & Graham, B. P. (2010). Encoding and retrieval in a model of the hippocampal CA1 microcircuit. *Hippocampus*, *20*(3), 423–446.

Cutsuridis, V., Graham, B. P., Cobb, S., & Vida, I. (Eds.). (2010). *Hippocampal microcircuits: A computational modeler's resource book* (Vol. 5). New York: Springer Science & Business Media.

Dayan, Peter, & Abbott, Laurence F. (2001). *Theoretical neuroscience*. Cambridge, MA: MIT Press.

Destexhe, A., Mainen, Z. F., & Sejnowski, T. J. (1994). Synthesis of models for excitable membranes, synaptic transmission and neuromodulation using a common kinetic formalism. *Journal of Computational Neuroscience*, *1*(3), 195–230.

Dingledine, R., Borges, K., Bowie, D., & Traynelis, S. F. (1999). The glutamate receptor ion channels. *Pharmacological Reviews*, *51*(1), 7–62.

Dinocourt, C., Petanjek, Z., Freund, T. F., Ben-Ari, Y., & Esclapez, M. (2003). Loss of interneurons innervating pyramidal cell dendrites and axon initial segments in the CA1 region of the hippocampus following pilocarpine-induced seizures. *Journal of Comparative Neurology*, *459*(4), 407–425.

Dittman, J. S., Kreitzer, A. C., & Regehr, W. G. (2000). Interplay between facilitation, depression, and residual calcium at three presynaptic terminals. *Journal of Neuroscience*, *20*(4), 1374–1385.

Ferrante, M., & Ascoli, G. A. (2015). Distinct and synergistic feedforward inhibition of pyramidal cells by basket and bistratified interneurons. *Frontiers in Cellular Neuroscience*, *9*.

Freund, T. F., & Buzsáki, G. Y. (1996). Interneurons of the hippocampus. *Hippocampus*, *6*(4), 347–470.

Fricker, D., & Miles, R. (2001). Interneurons, spike timing, and perception. *Neuron*, *32*(5), 771–774.

Gauck, V., & Jaeger, D. (2003). The contribution of NMDA and AMPA conductances to the control of spiking in neurons of the deep cerebellar nuclei. *Journal of Neuroscience*, *23*(22), 8109–8118.

Geng, K., & Marmarelis, V. Z. (2015). Pattern recognition of Hodgkin-Huxley equations by auto-regressive Laguerre-Volterra network. *BMC Neuroscience*, *16*(Supp. 1), 156.

Geng, K., & Marmarelis, V. Z. (2017). Methodology of recurrent Laguerre-Volterra network for modeling nonlinear dynamic systems. *IEEE Transactions on Neural Networks and Learning Systems*, *28*, 2196–2208.

Goldberg, E. M., & Coulter, D. A. (2013). Mechanisms of epileptogenesis: A convergence on neural circuit dysfunction. *Nature Reviews Neuroscience*, *14*(5), 337–349.

Golding, N. L., Kath, W. L., & Spruston, N. (2001). Dichotomy of action-potential backpropagation in CA1 pyramidal neuron dendrites. *Journal of Neurophysiology*, *86*(6), 2998–3010.

Hampson, R. E., Song, D., Chan, R. H., Sweatt, A. J., Riley, M. R., Gerhardt, G. A., . . . Deadwyler, S. A. (2012). A nonlinear model for hippocampal cognitive prosthesis: Memory facilitation by hippocampal ensemble stimulation. *IEEE Transactions on Neural Systems and Rehabilitation Engineering*, *20*(2), 184–197.

Hampson, R. E., Song, D., Opris, I., Santos, L. M., Shin, D, C., Gerhardt, G. A., . . . Deadwyler, S. A. (2013). Facilitation of memory encoding in primate hippocampus by a neuroprosthesis that promotes task-specific neural firing. *Journal of Neural Engineering*, *10*(6), 066013.

Häusser, M., Major, G., & Stuart, G. J. (2001). Differential shunting of EPSPs by action potentials. *Science*, *291*(5501), 138–141.

Heeger, D. (2000). Poisson model of spike generation. *Handout, Stanford University*, *5*, 1–13.

Henze, D. A., & Buzsaki, G. (2001). Action potential threshold of hippocampal pyramidal cells in vivo is increased by recent spiking activity. *Neuroscience*, *105*(1), 121–130.

Hodgkin, A. L., & Huxley, A. F. (1952). Propagation of electrical signals along giant nerve fibres. *Proceedings of the Royal Society of London. Series B, Biological Sciences*, *140*, 177–183.

Hu, E. Y., Bouteiller, J. M. C., Song, D., Baudry, M., & Berger, T. W. (2015). Volterra representation enables modeling of complex synaptic nonlinear dynamics in large-scale simulations. *Frontiers in Computational Neuroscience*, *9*.

Ising, E. (1925). Beitrag zur theorie des ferromagnetismus. *Zeitschrift für Physik*, *31*(1), 253–258.

Jacobs, J. (2014). Hippocampal theta oscillations are slower in humans than in rodents: Implications for models of spatial navigation and memory. *Philosophical Transactions of the Royal Society B–Biological Sciences*, *369*(1635), 20130304.

Johnston, D., Christie, B. R., Frick, A., Gray, R., Hoffman, D. A., Schexnayder, L. K., . . . Yuan, L. L. (2003). Active dendrites, potassium channels and synaptic plasticity. *Philosophical Transactions of the Royal Society B: Biological Sciences*, *358*(1432), 667–674.

Kandaswamy, U., Deng, P. Y., Stevens, C. F., & Klyachko, V. A. (2010). The role of presynaptic dynamics in processing of natural spike trains in hippocampal synapses. *Journal of Neuroscience*, *30*(47), 15904–15914.

Kapur, A., Lytton, W. W., Ketchum, K. L., & Haberly, L. B. (1997). Regulation of the NMDA component of EPSPs by different components of postsynaptic GABAergic inhibition: Computer simulation analysis in piriform cortex. *Journal of Neurophysiology*, *78*(5), 2546–2559.

Kirkpatrick, S., Gelatt Jr, C., & Vecchi, M. (1983). Optimization by simulated annealing. *Science*, *220*(4598), 671–680.

Klausberger, T. (2009). GABAergic interneurons targeting dendrites of pyramidal cells in the CA1 area of the hippocampus. *European Journal of Neuroscience*, *30*(6), 947–957.

Kleppe, I. C., & Robinson, H. P. (1999). Determining the activation time course of synaptic AMPA receptors from openings of colocalized NMDA receptors. *Biophysical Journal*, *77*(3), 1418–1427.

Klyachko, V. A., & Stevens, C. F. (2006). Excitatory and feed-forward inhibitory hippocampal synapses work synergistically as an adaptive filter of natural spike trains. *PLoS Biol.*, *4*(7), e207.

Kopell, N., Börgers, C., Pervouchine, D., Malerba, P., & Tort, A. (2010). Gamma and theta rhythms in biophysical models of hippocampal circuits. In V. Cutsuridis, B. P. Graham, S. Cobb, & I. Vida (Eds.), *Hippocampal Microcircuits* (pp. 423–457). New York: Springer.

Kullmann, D. M. (2011). Interneuron networks in the hippocampus. *Current Opinion in Neurobiology*, *21*(5), 709–716.

Kullmann, D. M., & Lamsa, K. P. (2007). Long-term synaptic plasticity in hippocampal interneurons. *Nature Reviews Neuroscience*, *8*(9), 687–699.

Larkum, M. E., Rioult, M. G., & Lüscher, H. R. (1996). Propagation of action potentials in the dendrites of neurons from rat spinal cord slice cultures. *Journal of Neurophysiology*, *75*(1), 154–170.

Leão, R. N., Mikulovic, S., Leão, K. E., Munguba, H., Gezelius, H., Enjin, A., . . . Kullander, K. (2012). OLM interneurons differentially modulate CA3 and entorhinal inputs to hippocampal CA1 neurons. *Nature Neuroscience*, *15*(11), 1524–1530.

Lega, B. C., Jacobs, J., & Kahana, M. (2012). Human hippocampal theta oscillations and the formation of episodic memories. *Hippocampus*, *22*(4), 748–761. doi:10.1002/hipo.20937

Lisman, J. E., & Jensen, O. (2013). The theta-gamma neural code. *Neuron*, *77*(6), 1002–1016.

Lüscher, H. R., & Larkum, M. E. (1998). Modeling action potential initiation and back-propagation in dendrites of cultured rat motoneurons. *Journal of Neurophysiology*, *80*(2), 715–729.

Maccaferri, G., & Lacaille, J. C. (2003). Interneuron diversity series: Hippocampal interneuron classifications—making things as simple as possible, not simpler. *Trends in Neurosciences*, *26*(10), 564–571.

Malenka, R. C., & Bear, M. F. (2004). LTP and LTD: An embarrassment of riches. *Neuron*, *44*(1), 5–21.

Mann, E. O., & Paulsen, O. (2007). Role of GABAergic inhibition in hippocampal network oscillations. *Trends in Neurosciences*, *30*(7), 343–349.

Marmarelis, P. Z., & Marmarelis, V. Z. (1978). *Analysis of physiological systems: The white-noise approach*. New York: Plenum Press.

Marmarelis, V. Z. (1997). Modeling methodology for nonlinear physiological systems. *Annals of Biomedical Engineering*, *25*(2), 239–251.

Marmarelis, V. Z. (2004). *Nonlinear dynamic modeling of physiological systems*. Hoboken, NJ: Wiley.

Marmarelis, V. Z., & Orme, M. E. (1993). Modeling of neural systems by use of neuronal modes. *IEEE Transactions on Biomedical Engineering*, *40*(11), 1149–1158, doi:10.1109/10.245633

Marmarelis, V. Z., Shin, D. C., Song, D., Hampson, R. E., Deadwyler, S. A., & Berger, T. W. (2013). Nonlinear modeling of dynamic interactions within neuronal ensembles using principal dynamic modes. *Journal of Computational Neuroscience*, *34*(1), 73–87.

Marmarelis, V. Z., Shin, D. C., Song, D., Hampson, R. E., Deadwyler, S. A., & Berger, T. W. (2014). On parsing the neural code in the prefrontal cortex of primates using principal dynamic modes. *Journal of Computational Neuroscience*, *36*(3), 321–337.

Marmarelis, V. Z., & Zhao, X. (1997). Volterra models and three-layer perceptrons. *IEEE Transactions on Neural Networks*, *8*(6), 1421–1433.

McBain, C. J., & Fisahn, A. (2001). Interneurons unbound. *Nature Reviews Neuroscience*, *2*(1), 11–23.

McMahon, L. L., & Kauer, J. A. (1997). Hippocampal interneurons express a novel form of synaptic plasticity. *Neuron*, *18*(2), 295–305.

Megias, M., Emri, Z. S., Freund, T. F., & Gulyas, A. I. (2001). Total number and distribution of inhibitory and excitatory synapses on hippocampal CA1 pyramidal cells. *Neuroscience*, *102*(3), 527–540.

Moser, M. B., Moser, E. I., Forrest, E., Andersen, P., & Morris, R. G. (1995). Spatial learning with a minislab in the dorsal hippocampus. *Proceedings of the National Academy of Sciences*, *92*(21), 9697–9701.

Müller, C., & Remy, S. (2014). Dendritic inhibition mediated by OLM and bistratified interneurons in the hippocampus. *Frontiers in Synaptic Neuroscience*, *6*, 23.

Nourani, Y., & Andresen, B. (1998). A comparison of simulated annealing cooling strategies. *Journal of Physics A: Mathematical and General*, *31*(41), 8373.

O'Keefe, J., & Burgess, N. (1996). Geometric determinants of the place fields of hippocampal neurons. *Nature*, *381*(6581), 425.

O'Keefe, J., & Nadel, L. (1978). *The hippocampus as a cognitive map*. Oxford: Clarendon Press.

Olypher, A. V., Lytton, W. W., & Prinz, A. A. (2012). Input-to-output transformation in a model of the rat hippocampal CA1 network. *Frontiers in Computational Neuroscience*, *6*, 57.

Otmakhova, N. A., Otmakhov, N., & Lisman, J. E. (2002). Pathway-specific properties of AMPA and NMDA-mediated transmission in CA1 hippocampal pyramidal cells. *Journal of Neuroscience*, *22*(4), 1199–1207.

Padurariu, M., Ciobica, A., Mavroudis, I., Fotiou, D., & Baloyannis, S. (2012). Hippocampal neuronal loss in the CA1 and CA3 areas of Alzheimer's disease patients. *Psychiatria Danubina*, *24*(2), 152–158.

Paninski, Liam. (2004). Maximum likelihood estimation of cascade point-process neural encoding models. *Network: Computation in Neural Systems 15*, 243–262.

Paz, J. T., & Huguenard, J. R. (2015). Microcircuits and their interactions in epilepsy: Is the focus out of focus? *Nature Neuroscience*, *18*(3), 351–359.

Pouille, F., & Scanziani, M. (2004). Routing of spike series by dynamic circuits in the hippocampus. *Nature*, *429*(6993), 717–723.

Quiroga, R. Q. (2012). Concept cells: The building blocks of declarative memory functions. *Nature Reviews Neuroscience*, *13*(8), 587.

Regehr, W. G. (2012). Short-term presynaptic plasticity. *Cold Spring Harbor Perspectives in Biology*, *4*(7), a005702.

Sandler, R. A., Song, D., Hampson, R. E., Deadwyler, S. A., Berger, T. W., & Marmarelis, V. Z. (2015a). Hippocampal closed-loop modeling and implications for seizure stimulation design. *Journal of Neural Engineering*, *12*(5), 056017.

Sandler, R. A., Song, D., Hampson, R. E., Deadwyler, S. A., Berger, T. W., & Marmarelis, V. Z. (2015b). Model-based assessment of an in-vivo predictive relationship from CA1 to CA3 in the rodent hippocampus. *Journal of Computational Neuroscience*, *38*(1), 89–103, doi:10.1007/s10827-014-0530-8

Saudargiene, A., Cobb, S., & Graham, B. P. (2015). A computational study on plasticity during theta cycles at Schaffer collateral synapses on CA1 pyramidal cells in the hippocampus. *Hippocampus*, *25*(2), 208–218.

Scoville, W. B., & Milner, B. (1957). Loss of recent memory after bilateral hippocampal lesions. *Journal of Neurology, Neurosurgery, and Psychiatry*, *20*(1), 11–21.

Sik, A., Penttonen, M., Ylinen, A., & Buzsáki, G. (1995). Hippocampal CA1 interneurons: An in vivo intracellular labeling study. *Journal of Neuroscience*, *15*(10), 6651–6665.

Small, S. A., Schobel, S. A., Buxton, R. B., Witter, M. P., & Barnes, C. A. (2011). A pathophysiological framework of hippocampal dysfunction in ageing and disease. *Nature Reviews Neuroscience*, *12*(10), 585–601.

Song, D., Chan, R. H., Marmarelis, V. Z., Hampson, R. E., Deadwyler, S. A., & Berger, T. W. (2007). Nonlinear dynamic modeling of spike train transformations for hippocampal-cortical prostheses. *IEEE Transactions on Biomedical Engineering*, *54*(6 Pt. 1), 1053–1066, doi:10.1109/TBME.2007.891948

Song, D., Marmarelis, V. Z., & Berger, T. W. (2009). Parametric and non-parametric modeling of short-term synaptic plasticity. Part I: Computational study. *Journal of Computational Neuroscience*, *26*(1), 1–19.

Song, D., Robinson, B., Hampson, R., Marmarelis, V., Deadwyler, S., & Berger, T. (2016, Aug. 30). Sparse large-scale nonlinear dynamical modeling of human hippocampus for memory prostheses. *IEEE Transactions on Neural Systems and Rehabilitation Engineering*, doi:10.1109/TNSRE.2016.2604423

Song, D., Wang, H., Tu, C. Y., Marmarelis, V. Z., Hampson, R. E., Deadwyler, S. A., & Berger, T. W. (2013). Identification of sparse neural functional connectivity using penalized likelihood estimation and basis functions. *Journal of Computational Neuroscience*, *35*(3), 335–357, doi:10.1007/s10827-013-0455-7

Spruston, N. (2008). Pyramidal neurons: Dendritic structure and synaptic integration. *Nature Reviews Neuroscience*, *9*(3), 206–221.

Spruston, N., Schiller, Y., Stuart, G., & Sakmann, B. (1995). Activity-dependent action potential invasion and calcium influx into hippocampal CA1 dendrites. *Science*, *268*(5208), 297.

Stuart, G., Spruston, N., Sakmann, B., & Häusser, M. (1997). Action potential initiation and backpropagation in neurons of the mammalian CNS. *Trends in Neurosciences*, *20*(3), 125–131.

Truccolo, W., Eden, U. T., Fellows, M. R., Donoghue, J. P., & Brown, E. N. (2005). A point process framework for relating neural spiking activity to spiking history, neural ensemble, and extrinsic covariate effects. *Journal of Neurophysiology*, *93*(2), 1074–1089.

Tsien, J. Z., Huerta, P. T., & Tonegawa, S. (1996). The essential role of hippocampal CA1 NMDA receptor–dependent synaptic plasticity in spatial memory. *Cell*, *87*(7), 1327–1338.

Tulving, E., & Markowitsch, H. J. (1998). Episodic and declarative memory: Role of the hippocampus. *Hippocampus*, *8*(3), 198–204.

Wang, Z., Song, D., & Berger, T. W. (2002). Contribution of NMDA receptor channels to the expression of LTP in the hippocampal dentate gyrus. *Hippocampus*, *12*(5), 680–688.

Watrous, A. J., Fried, I., & Ekstrom, A. D. (2011). Behavioral correlates of human hippocampal delta and theta oscillations during navigation. *Journal of Neurophysiology*, *105*(4), 1747–1755, doi:10.1152/jn.00921.2010

Watrous, A. J., Lee, D. J., Izadi, A., Gurkoff, G. G., Shahlaie, K., & Ekstrom, A. D. (2013). A comparative study of human and rat hippocampal low-frequency oscillations during spatial navigation. *Hippocampus*, *23*(8), 656–661, doi:10.1002/hipo.22124

West, M. J., Coleman, P. D., Flood, D. G., & Troncoso, J. C. (1994). Differences in the pattern of hippocampal neuronal loss in normal ageing and Alzheimer's disease. *Lancet*, *344*(8925), 769–772.

Whitlock, J. R., Heynen, A. J., Shuler, M. G., & Bear, M. F. (2006). Learning induces long-term potentiation in the hippocampus. *Science*, *313*(5790), 1093–1097.

Womelsdorf, T., Valiante, T. A., Sahin, N. T., Miller, K. J., & Tiesinga, P. (2014). Dynamic circuit motifs underlying rhythmic gain control, gating and integration. *Nature Neuroscience*, *17*(8), 1031–1039.

Wu, F.-Y. (1982). The Potts model. *Reviews of Modern Physics*, *54*(1), 235.

Zanos, T. P., Courellis, S. H., Berger, T. W., Hampson, R. E., Deadwyler, S. A., & Marmarelis, V. Z. (2008). Nonlinear modeling of causal interrelationships in neuronal ensembles. *IEEE Transactions on Neural Systems and Rehabilitation Engineering*, *16*(4), 336–352, doi:10.1109/TNSRE.2008.926716

Zucker, R. S., & Regehr, W. G. (2002). Short-term synaptic plasticity. *Annual Review of Physiology*, *64*(1), 355–405.